

# GPS phase scintillation at high latitudes during the geomagnetic storm of March 17-18, 2015

P. Prikryl<sup>1,2</sup>, R. Ghoddousi-Fard<sup>3</sup>, J. M. Weygand<sup>4</sup>, A. Viljanen<sup>5</sup>, M. Connors<sup>6</sup>, D. W. Danskin<sup>2</sup>, P. T. Jayachandran<sup>1</sup>, K. S. Jacobsen<sup>7</sup>, Y. L. Andalsvik<sup>7</sup>, E. G. Thomas<sup>8,9</sup>, J. M. Ruohoniemi<sup>8</sup>, T. Durgonics<sup>10</sup>, K. Oksavik<sup>11,12</sup>, Y. Zhang<sup>13</sup>, E. Spanswick<sup>14</sup>, M. Aquino<sup>15</sup>, V. Sreeja<sup>15</sup>

<sup>1</sup>Physics Department, University of New Brunswick, Fredericton, NB

<sup>2</sup>Geomagnetic Laboratory, Natural Resources Canada, Ottawa, ON

<sup>3</sup>Canadian Geodetic Survey, Natural Resources Canada, Ottawa, ON

<sup>4</sup>Institute of Geophysics and Planetary Physics, University of California, Los Angeles, CA, USA

<sup>5</sup>Finnish Meteorological Institute, Helsinki, Finland

<sup>6</sup>Athabasca University, Edmonton, Alberta, Canada

<sup>7</sup>Norwegian Mapping Authority, Hønefoss, Norway

<sup>8</sup>Bradley Department of Electrical and Computer Engineering, Virginia Tech, Blacksburg, VA, USA

<sup>8</sup>Thayer School of Engineering, Dartmouth College, Hanover, NH, USA

<sup>10</sup>Technical University of Denmark, National Space Institute, Kongens Lyngby, Denmark

<sup>11</sup>Birkeland Centre for Space Science, Department of Physics and Technology, University of Bergen, Bergen, Norway

<sup>12</sup>The University Centre in Svalbard, Longyearbyen, Norway

<sup>13</sup>Johns Hopkins University Applied Physics Laboratory, Laurel, MD, USA

<sup>14</sup>Department of Physics and Astronomy, University of Calgary, AB, Canada

<sup>15</sup>Nottingham Geospatial Institute, University of Nottingham, Nottingham, UK

This article has been accepted for publication and undergone full peer review but has not been through the copyediting, typesetting, pagination and proofreading process which may lead to differences between this version and the Version of Record. Please cite this article as doi: 10.1002/2016JA023171

## **Abstract**

The geomagnetic storm of March 17-18, 2015 was caused by the impacts of a coronal mass ejection and a high-speed plasma stream from a coronal hole. The high-latitude ionosphere dynamics is studied using arrays of ground-based instruments including GPS receivers, HF radars, ionosondes, riometers and magnetometers. The phase scintillation index is computed for signals sampled at a rate of up to 100 Hz by specialized GPS scintillation receivers supplemented by the phase scintillation proxy index obtained from geodetic-quality GPS data sampled at 1 Hz. In the context of solar wind coupling to the magnetosphere-ionosphere system, it is shown that GPS phase scintillation is primarily enhanced in the cusp, the tongue of ionization that is broken into patches drawn into the polar cap from the dayside storm-enhanced plasma density, and in the auroral oval. In this paper we examine the relation between the scintillation and auroral electrojet currents observed by arrays of ground-based magnetometers as well as energetic particle precipitation observed by the DMSP satellites. Equivalent ionospheric currents are obtained from ground magnetometer data using the spherical elementary currents systems technique that has been applied over the ground magnetometer networks in North America and North Europe. The GPS phase scintillation is mapped to the poleward side of strong westward electrojet and to the edge of the eastward electrojet region. Also, the scintillation was generally collocated with fluxes of energetic electron precipitation observed by DMSP satellites with the exception of a period of pulsating aurora when only very weak currents were observed.

## **1. Introduction**

Ionospheric irregularities cause rapid fluctuations of radio wave amplitude and phase called scintillation that can degrade GPS positional accuracy and affect the performance of radio communication and navigation systems [Skone and de Jong, 2000; Aquino et al., 2007; Kintner et al., 2007; Jacobsen and Dähnn, 2014; Jacobsen and Andalsvik, 2015]. The total electron content (TEC) as observed by GPS becomes particularly disturbed during geomagnetic storms caused by the impacts of interplanetary coronal mass ejections (ICMEs) compounded by high-speed plasma streams from coronal holes. In the context of solar wind coupling to the magnetosphere-ionosphere system, it has been shown that GPS phase scintillation is primarily enhanced in the cusp, where a tongue of ionization (TOI) is broken

into patches and is drawn into the polar cap from the dayside storm-enhanced plasma density (SED) [Aaron, 1997; Aaron *et al.*, 2000; Basu *et al.*, 1987, 1995, 1998; Spogli *et al.*, 2009; Li *et al.*, 2010; Prikryl *et al.*, 2011a, 2011b, 2014, 2015a,b; Moen *et al.*, 2013; Sreeja and Aquino, 2014; van der Meer *et al.*, 2014; Jin *et al.*, 2015; Oksavik *et al.*, 2015]. In the auroral oval, GPS scintillation has been observed during energetic particle precipitation events, substorms and pseudo-breakups [Skone *et al.*, 2008; Kinrade *et al.*, 2013; Prikryl *et al.*, 2013a, 2013b] and correlated with ground magnetic field perturbations [Skone and Cannon, 1999; Prikryl *et al.*, 2011a; Ghoddousi-Fard *et al.*, 2015]. The present paper focuses on the GPS phase scintillation in relation to the auroral electrojets as observed in the North American and North European sectors during this geomagnetic storm.

## 2. Instruments and techniques

In the Canadian Arctic, the GPS phase and amplitude scintillation is monitored by the Canadian High Arctic Ionospheric Network (CHAIN) consisting of GPS Ionospheric Scintillation and TEC Monitors (GISTMs) that are configured to record the power and phase of the L1 signal at a 50-Hz sampling rate. The original CHAIN (Jayachandran *et al.*, 2009) consisted of NovAtel GSV4004B receivers that are capable of tracking up to 10 GPS signals at the L1 frequency (1575.42 MHz) and the L2 frequency (1227.6 MHz). Starting in 2014, CHAIN has been expanded by adding new stations equipped with Septentrio PolaRxS multi-GNSS receivers capable of tracking up to 30 satellites including GPS, GLONASS and Galileo.

In the European sector, the Norwegian Mapping Authority (NMA) operates 10 GISTMs and a dense nationwide network of about 185 1-Hz geodetic receivers. In the Svalbard region, the Birkeland Centre for Space Science operates four NovAtel GPStation-6 multi-GNSS receivers at Ny-Ålesund, Longyearbyen, Hopen, and Bjørnøya [Oksavik *et al.*, 2015; van der Meer *et al.*, 2015]. The receivers track signals from GPS (L1/L2/L2C/L5), GLONASS (L1/L2), and Galileo (E1/E5a/E5b/Alt-BOC). Scintillation indices  $\sigma_\phi$  and  $S4$ , based on standard deviation of phase and amplitude over 60 s intervals, are output from the receiver. Only GPS/L1/L2) signals are used in the present paper. The receivers also provide the TEC and rate of TEC Index (ROTI) (not used in this study). Raw data of the amplitude and phase are available at a 50-Hz resolution. Additional GSV4004B and Septentrio PolaRxS receivers

are operated in Norway, Cyprus and in the UK by the Nottingham Geospatial Institute (NGI) of the University of Nottingham.

At the Canadian Geodetic Survey of Natural Resources Canada about 150 globally distributed 1-Hz GPS stations (mostly those of the RT-IGS network with additional stations over Canadian region) are used in near-real-time to derive, among other statistics and products [Ghoddousi-Fard *et al.*, 2011, Ghoddousi-Fard and Lahaye, 2016], L1-L2 inter-frequency phase rate variations by means of mapped-to-zenith standard deviation of delta phase rate (sDPR) over 30 sec. For further details we refer the reader to Ghoddousi-Fard *et al.* [2013]. The Technical University of Denmark, National Space Institute (DTU Space) contributed high-rate GPS receivers of the Greenland GPS Network (GNET). GNET consists of 62 GPS stations (11 of these sample at 1 Hz) that are distributed around the Greenland inland ice. GPS receivers sampling at a 1-Hz rate complement the GISTMs by providing the sDPR proxy scintillation index.

The Super Dual Auroral Radar Network (SuperDARN) [Greenwald *et al.*, 1995, Chisham *et al.*, 2007] is used to map ionospheric convection in the northern hemisphere. The TEC data downloaded from Madrigal, an upper atmospheric science database at Haystack Observatory (<http://madrigal.haystack.mit.edu/madrigal/>), are used to make GPS TEC maps [Thomas *et al.*, 2013] that are also available online (<http://vt.superdarn.org>).

Equivalent ionospheric currents (EICs) are obtained from ground magnetometer data using the spherical elementary currents systems (SECS) technique developed by Amm and Viljanen [1999] that has been applied over the entire North American ground magnetometer network by Weygand *et al.* [2011]. The SECS technique defines elementary divergence-free and curl-free current systems. The divergence-free system with currents that flow entirely within the ionosphere causes a magnetic field on the ground. The curl-free system whose divergences represent the currents normal to the ionosphere produces no field below the ionosphere [Landau *et al.*, 2015]. For this study the SEC method calculates the divergence-free currents and from those the spherical elementary current amplitudes are obtained. The SECS method also makes it possible to roughly estimate field-aligned currents under the assumption of no conductance gradients perpendicular to the ionospheric electric field [Weygand *et al.*, 2016].

While the EICs/SECS maps were inferred at the minimum resolution of the magnetometer database (10 s), in this paper we use data decimated to 60 s.

Figure 1 shows the various GNSS receivers as well as the arrays of magnetometers including those operated by the Natural Resources Canada, the Canadian Array for Realtime Investigations of Magnetic Activity (CARISMA) [Mann *et al.*, 2008] of the Canadian GeoSpace Monitoring (CGSM) program (Liu, 2005), the Geophysical Institute Magnetometer Array (GIMA) ([www.asf.alaska.edu/magnetometer/](http://www.asf.alaska.edu/magnetometer/)), the Greenland array operated by Technical University of Denmark ([www.space.dtu.dk](http://www.space.dtu.dk)) and IMAGE (<http://space.fmi.fi/image/>).

The Defense Meteorological Satellite Program (DMSP) satellites provided particle data to support the scintillation study. The DMSP particle detectors were designed by the Dave Hardy of Air Force Research Laboratory, and data are obtained from the Johns Hopkins University Applied Research Laboratory (<http://sd-www.jhuapl.edu/Aurora/>). Data from a special sensor ultraviolet scanning imager (SSUSI) onboard the DMSP F16 and F17 satellites (<http://sd-www.jhuapl.edu/Aurora/>) were used to produce partial images of the auroral oval [Paxton *et al.* 2002; Zhang and Paxton 2008].

The ground-based all-sky imager (ASI) stations support the NASA Time History of Events and Macroscale Interactions during Substorms (THEMIS) project [Mende *et al.*, 2008]. Figure 1 shows field-of-views of four ASIs.

### **3. Geomagnetic storm of March 17-18, 2015**

#### **3.1. Solar wind and geomagnetic conditions**

An interplanetary coronal mass ejection (ICME) ahead of a high-speed plasma stream from a coronal hole led to a geo-effective configuration in the solar wind [Kataoka *et al.*, 2015] that resulted in a severe geomagnetic storm on March 17-18, 2015. In agreement with the conclusions by Kamide and Kusano [2015], Kataoka *et al.* [2015] pointed out that the storm involved a two-step development, the first driven by the southward IMF in the compressed sheath region, and the second driven by the southward IMF in the magnetic cloud. During

this day the  $Kp$  index reached a value of 8 and the auroral electrojet ( $AE$ ) index exceeded 2000 nT. Figure 2a-f shows, from top to bottom, 1-min averages of the solar wind velocity,  $V_{sw}$ , the IMF components  $B_y$  and  $B_z$ , total magnitude,  $B$ , and proton density,  $n_p$ , and temperature,  $T_p$ , from the OMNI data set projected to the subsolar bow shock. The upstream interplanetary (IP) shock is indicated by the vertical dotted line at 04:45 UT. The IMF  $B_z$  initially turned strongly northward (corresponding to positive excursion in  $SYM-H$ , signaling initial phase of the storm) and then sharply southward, remaining mostly southward for the rest of the day as the storm intensified. Figure 2g shows the hourly occurrence of phase scintillation ( $\sigma_\phi > 0.1$  rad) observed by CHAIN, while Figure 2h shows provisional geomagnetic indices. The  $AE$  index peaked at 2298 nT at 13:58 UT and  $SYM-H$  dipped to -234 nT at 22:47 UT.

### 3.2. Ionospheric irregularities at high latitudes

The ROTI measured by more than 2500 GNSS receivers [Cherniak *et al.*, 2015] revealed considerable dynamics of ionospheric irregularities on a global scale. Significant increases in the intensity of irregularities in the polar cap of both hemispheres were associated with the formation and evolution of SED/TOI and polar patches. In the northern hemisphere, a band of intense auroral ionospheric irregularities that expanded equatorward beyond  $\sim 45^\circ\text{N}$  of geographic latitude was associated with processes related to enhanced auroral particle precipitation [Cherniak *et al.*, 2015]. Jacobsen and Andalsvik [2016] studied the irregularities in the TEC in relation to the auroral electrojet currents during the geomagnetic storm of March 17-18, 2015. They showed that the most intense disturbances of GNSS signals characterized by ROTI occurred on the poleward side of poleward-moving current regions over North Europe.

The hourly occurrences of phase scintillation with  $\sigma_\phi > 0.1$  radians that are shown in Figure 2g for CHAIN stations at Eureka (EURC), Cambridge Bay (CBBC) and Sanikiluaq (SANC) approximately represent the central polar cap, cusp and auroral zone, respectively. Scintillation is often observed in CBBC even during geomagnetically less disturbed conditions, either in the cusp or in a contracted auroral oval. The onset of GPS phase scintillation in the expanded auroral oval followed the southward turning of the IMF about 2 hours after the IP shock (shown in dotted vertical line) that was associated with a strong

northward IMF. Several hours later, after 12:00 UT, under the influence of the magnetic cloud that was characterized by a decrease in proton temperature (Figure 2f) and strong southward IMF, the GPS scintillation occurrence increased in the auroral zone, cusp and the central polar cap.

Figures 3a and 3b show the occurrence of phase scintillation above comparable thresholds [Prikryl *et al.*, 2013a] of  $\sigma_\phi > 0.1$  rad or  $sDPR > 2$  mm/s as a function of the Altitude Adjusted Corrected Geomagnetic (AACGM) latitude and magnetic local time (MLT) before and during the geomagnetic storm, respectively. Assuming an ionospheric pierce point (IPP) height of 350 km, the scintillation occurrence is defined as  $100 \times N(\sigma_\phi > 0.1) / N_{\text{tot}}$ , where  $N$  is the number of cases when phase scintillation index exceeded a given threshold and  $N_{\text{tot}}$  is the total number of data points with IPPs in the bin of 0.25 hour MLT  $\times$  1° AACGM latitude. Boundaries of the Feldstein statistical auroral oval [Holtzworth and Meng, 1975] for quiet and disturbed conditions are shown in Figures 3a and 3b, respectively. In Figure 3a, the data for all available GISTMs combined with 1-Hz GPS receivers from 04:00 UT on March 16 to 03:59 UT on March 17 are used to show 24 h in MLT before the storm, when the IMF was pointing northward. As a result, scintillation was confined within the polar cap and small auroral oval. In Figure 3b, the scintillation data from 04:00 UT on March 17 to 03:59 UT on March 18 are used to show 24 h in MLT. During the storm, scintillation occurrence was strongly enhanced on the dayside in the cusp and SED region, a source of TOI plasma fragmented into patches that were drawn into the polar cap. The IMF  $B_y$  was initially dawnward (negative) for several hours before it switched to duskward at ~11:00 UT. As a result, TOI entry was initially through the cusp in the pre-noon sector, from where a duskward and antisunward convection pulled a fragmented TOI into the polar cap.

Figure 4a shows SuperDARN convection and potential maps at 09:10 UT on March 17 during southward and dawnward IMF. After a period of a strong southward IMF the convection zone expanded significantly. The Heppner–Maynard (H-M) boundary [Imber *et al.*, 2013] moved to 50° of the AACGM latitude. The convection intensified with a potential difference across the polar cap of  $\Phi_{\text{PC}} = 79$  kV. The IPPs at 350 km (black dots) with  $\sigma_\phi > 0.1$  rad and  $sDPR > 2$  mm/s mapped to the cusp and the dawn convection cell, particularly in the midnight and post-midnight sector. At this time there was very sparse GPS data coverage of the dusk cell except around the noon near the cusp. To avoid crowding of IPPs over

Scandinavia, only 33 NMA 1-Hz GPS receivers evenly covering Norway (Figure 1) are used in Figures 4, 5 and 6. However, the whole data set for 185 NMA stations is used in Figures 3 and 12.

Figure 4b shows 5-min median-filtered TEC maps overlaid with the electrostatic potential contours and IPPs for cases of phase scintillation  $\sigma_\phi > 0.1$  rad and  $sDPR > 2$  mm/s. The dotted line shows the solar terminator at an F-region height. The map shows enhanced TEC in the nightside auroral oval poleward of a depleted TEC in the main trough centered at about  $50^\circ$  AACGM latitude. The IPPs with the highest level of scintillation are located just poleward of the enhanced TEC and the return convection in the post-midnight sector. Figure 4c shows the IPPs by scaled circles to indicate scintillation intensity. We refer to threshold values shown in the legend to approximately define weak ( $\sigma_\phi < 0.25$  rad;  $sDPR < 5$  mm/s), moderate ( $0.25 < \sigma_\phi < 0.5$  rad;  $5 < sDPR < 10$  mm/s) and strong ( $\sigma_\phi > 0.5$  rad;  $sDPR > 10$  mm/s) scintillation. At the lowest latitude near the main trough around midnight, a dense cloud of IPPs is collocated with a subauroral polarization stream (SAPS) [Prikryl *et al.*, 2015c]. At this time, only a weak to moderate scintillation is observed on the dayside where it is collocated with a fragmented TOI was drawn through the cusp from high TEC in the SED region in the pre-noon sector. Also, weak to moderate scintillation is observed in the night-side of polar cap.

After the IMF  $B_y$  reversed polarity to duskward (positive) the cusp shifted to the post-noon sector (Figure 5). At this time, then TOI was drawn from high TEC in the post-noon SED region (Figure 5b). Moderate scintillation was collocated with the TOI but quite strong scintillation was observed at the poleward edge of the SED at  $\sim 15:00$  MLT (Figure 5c). In the central polar cap, only weak scintillation was observed. In the auroral zone, strong scintillation was collocated with intense return convection in the dawn convection cell.

At 18:30 UT on March 17 (Figure 6), duskward and anti-sunward convection on the dayside intensified drawing copious patches into the polar cap. Moderate to strong scintillation was observed at the poleward edge of the SED region, in the cusp and collocated with TOI fragmented into patches. Further poleward in the polar cap the scintillation level was reduced, although it was enhanced in the night side polar cap, where anti-sunward convection is expected to carry polar cap patches towards the nightside auroral oval. In the dusk auroral

zone, scintillation was strong but no convection was observed due to a lack of radar backscatter from F-region irregularities. Finally, weak scintillation extended to subauroral latitudes down to 50° AACGM latitude near the poleward edge of the main trough at 19-20 MLT.

### 3.3. GPS phase scintillation in relation to auroral currents

In this section we apply the SECS technique to obtain horizontal equivalent currents and the vertical current amplitudes from an array of ground magnetometers seeking a comparison with GPS phase scintillation occurrence in relation with EICs. For the inversion technique we use ground magnetometer data from 77 stations in the North American sector (11 stations in western Greenland). Following *Weygand et al.* [2011], for each of these stations the quiet-time background from March 2015 is subtracted from the measured field to give the disturbance component which determines the EICs. To calculate the quiet-time background, intervals of relatively smooth magnetometer data (varying in length from an hour to a whole day) are selected with an automated routine from the  $B_x$  and  $B_y$  components for nearly every day over a three month period. These intervals are then averaged together and smoothed to create one 24 h quiet-time background interval. Typically the quiet-time backgrounds are as smooth as, or smoother than, the average of the 5 quietest days per month. See *Weygand et al.* [2011] for more details on the derivation of the quiet-time background.

Figure 7a shows a horizontal EIC mapped at 09:10 UT to be compared with Figure 4. At this time, strong westward electrojet currents are seen across the continent between about 50 and 60° geographic latitude from southern Greenland to Alaska. At high latitudes poleward of ~65° geographic latitude, eastward EICs appear to dominate. However, the magnetometer coverage is poor around 120°W poleward of ~65°N as well as on the east coast around 60°W from Labrador to Baffin Island to place much weight on the inversion results there. The westward electrojet pattern compares reasonably well with the dawn convection cell shown in AACGM coordinates (Figure 4a). The westward electrojet approximately traces a dividing line between regions of up and down  $J_z$  currents shown in Figure 7b. As shown by *Weygand et al.* [2016] these up and down SECS currents indicate the region-1 and region-2 currents, respectively. The boundary between the region-1 and region-2 currents helps to identify the

approximate location of the particle precipitation region [Weygand *et al.*, 2016; and references therein].

IPPs of strong GPS phase scintillation are largely collocated with the westward electrojet currents but are also near the reversal boundary to eastward EICs (Figure 7a). A height of 110 km is assumed for IPPs (see, discussion in Section 4) with GPS scintillation that are superposed on currents in Figures 7 and 8. In relation to SECS  $J_z$ , there is a tendency of strong scintillation to map to upward or downward  $J_z$ , or near the reversal boundaries between downward and upward  $J_z$ , as would be expected for scintillation being caused by ionization due to precipitating electrons. A similar relation to currents can be seen in Figure 8 at a later UT of 13:25. The strongest scintillation is collocated with an intense westward electrojet or its poleward border but also with the eastward electrojet at the eastern edge of the array (over Greenland) (Figure 8a). In terms of the vertical currents, the IPPs with strong scintillation are closely collocated with both upward and downward  $J_z$  (Figure 8b). At this time, the DMSP F17 satellite pass with the auroral imager SSUSI observed UV (LBH bands of N2) aurora that is mapped as a function of AACGM latitude and MLT in Figure 9. The scintillation IPPs are superposed for the time interval of 13:25-13:30 UT also shown in Figure 8. The strong scintillation is mostly collocated with, or near the edge of, the auroral emissions that were scanned approximately during the same time interval.

Figure 10a shows the GPS phase scintillation occurrence as a function of AACGM latitude and UT for GPS receiver stations located between 260° and 300° geographic longitude overlaid with contours of  $J_y$  current. The  $J_y$  current shown in Figure 10b is an average over the longitude sector between 267° and 295° with EICs transformed to geomagnetic coordinates using the magnetic declination at each grid cell. To conform to the 15-min grid span used for the scintillation occurrence map, the west-to-east  $J_y$  current component is averaged over 15 min (mean of 15 values using the 10-s EICs data decimated to one value per minute). In the auroral zone, the highest occurrence of GPS phase scintillation is generally collocated with strong EICs particularly the poleward part of the westward electrojet or near the edge of the eastward electrojet regions.

Figure 10b shows the EIC contours color-coded with the magnitude of the  $J_y$  current. Superposed on the EIC contour plot are tracks of the DMSP F16 and F17 satellites when they crossed the longitude sector between  $260^\circ$  and  $300^\circ\text{E}$ . The tracks are color-coded with observed energy flux of 10 keV electrons. It is noted that, similar to scintillation, the energetic electron fluxes are elevated at the edges of the westward or eastward electrojets, predominantly on their poleward side. An exception are two passes (F16 and F17) showing high fluxes of energetic electrons between 11:00 and 12:00 UT when no scintillation and only weak EICs were observed equatorward of  $72^\circ\text{N}$  of AACGM latitude. This was a period when the IMF turned once again northward (Figure 2c) temporarily stalling the development of the geomagnetic storm and disrupting two-cell ionospheric convection and when mid-latitude radars across North America observed westward propagating ULF waves. Figure 11a shows line-of-sight velocity (LoS) observed by the Fort Hays East radar beam 1 as a function of AACGM latitude on March 17. Before the arrival of the IP shock ( $\sim 04:46$  UT) the radar observed near-zero velocity due to ground scatter. With the arrival of the shock there was an initial period of low-velocity fluctuation between  $50^\circ$  and  $64^\circ$  latitude that was due to subauroral ionospheric scatter. Because the IMF was northward during this period (Fig. 2c), the auroral oval and convection zone contracted. It was only after 06:00 UT when the IMF turned sharply southward that the auroral oval and the dawn convection cell came into the radar field-of-view. The initially toward-the-radar LoS flow (coded blue) that was observed in the midnight sector gradually reversed to away LoS flow (coded red) in the post-midnight and dawn sectors. However, there was a temporary cessation of organized large-scale flow and an onset of strong pulsations due to ULF waves after  $\sim 10:30$  UT. At this time, THEMIS ASIs in the auroral zone across Canada (Figure 11) observed pulsating aurora, which is known to be caused by energetic particle precipitation. Figure 11c shows snapshots of pulsating aurora observed by ASIs in White horse, Fort Smith, Athabasca and Pinawa. The ASI data from Pinawa are processed into a keogram with two periods of pulsating aurora approximately indicated by circles (Figure 11b). The lack of GPS scintillation during these periods suggests that pulsating auroras do not produce kilometer size irregularities and steep electron density gradients. However, to exclude the possibility of scintillation caused by smaller sizes would require higher sampling rate data.

Figure 12a shows the GPS phase scintillation occurrence for GPS receiver stations located between 350 and 30°E geographic longitude overlaid with contours of EIC  $J_y$  current inverted from the IMAGE magnetometer data from the North European sector. Similarly to the North American sector (Figure 10), the scintillation is observed along the poleward border of the eastward electrojet and collocated with the regions of westward electrojet. A couple of DMSP passes show energetic electron flux enhancements, one collocated with the westward electrojet, and the second at the poleward edge of the eastward electrojet. In both cases the scintillation was also observed in those regions.

#### 4 Discussion and Summary

The solar wind coupling to the magnetosphere–ionosphere system results in a highly structured and dynamic high-latitude ionosphere causing GPS scintillation. On March 16, the day prior to the storm, the GPS scintillation that was largely confined to the polar cap was caused by sun-aligned polar cap arcs that are a consequence of northward IMF (Figure 2c) [Prikryl *et al.*, 2015a]. In contrast, during the storm when the  $B_z$  was southward, scintillation occurrence was strongly enhanced in the cusp and SED regions. In the polar cap, the scintillation was caused by TOI fragmented into patches. Because the IMF  $B_y$  controls the dawn–dusk asymmetry of ionospheric convection, the scintillation occurrence band associated with TOI spans the polar cap from the post-noon to post-midnight sector for IMF  $B_y < 0$  and from the post-midnight to post-noon sector for IMF  $B_y > 0$  [Prikryl *et al.*, 2015c]. The scintillation occurrence on the dayside and in the polar cap, as shown in Figure 3b, was a superposition of the two states that were discussed in details for two storms by the latter authors. The IMF  $B_y$  was initially dawnward ( $< 0$ ) for several hours before it switched to duskward ( $> 0$ ) at ~11:00 UT and thus TOI/patches entry switched from initially pre-noon cusp (Figure 4) to post-noon cusp (Figure 5 and 6). As a result, the scintillation occurrence map, as a function of MLT (Figure 3b), shows a composite of the two states resulting in an approximate symmetry about the noon of the dayside scintillation occurrence in the cusp and polar cap.

It is common to approximate the ionosphere as a relatively thin phase-changing shell at 350 km altitude to map the scintillation IPPs and this is quite appropriate with polar cap patches. However, the altitude of GPS scintillation-generating irregularities is often difficult to determine. It is expected that scintillation is caused by F-region irregularities at low latitudes where the processes of irregularity generation differ from those at high latitudes. At low latitudes, particularly near the equatorial ionization anomaly, the scintillation-causing irregularities with scale sizes of a few hundreds of meters are generated by large F-region structures (plasma bubbles) and form after sunset [Sreeja *et al.*, 2011; de Paula *et al.*, 2015]. In contrast, at high latitudes, scintillation-causing irregularities can be produced by a variety of auroral and polar cap phenomena, including cusp dynamics, auroral particle precipitation, auroral blobs and polar cap patches [Moen *et al.*, 2013; van der Meeren *et al.*, 2014; 2015; Oksavik *et al.*, 2015] that produce scintillation-causing irregularities at different altitudes. For example, in the case of particle precipitation with different energy causing emissions 557.7 and 630.0 nm, the GPS IPPs have been projected to 150 and 250 km altitudes on the mapped green 557.7-nm and red 630.0-nm emissions, respectively [van der Meeren *et al.*, 2014; 2015]. Other studies used slightly different altitudes.

In the brief survey of scintillation-causing irregularities in the context of ionospheric signatures of solar wind coupling (Figures 3 to 6) we assumed an IPP height of 350 km. This may be appropriate for density patches in the polar cap, the cusp and the density gradients at the poleward edge of SED region. However, in the auroral oval, scintillation is found collocated with energetic particle precipitation causing bright auroras that maximizes at much lower altitudes. In Section 3.3 (Figures 7 to 12), we examine the relation between the scintillation occurrence and the ionospheric currents (auroral electrojets and field-aligned currents) as well as auroral precipitation and thus we assume IPPs at 110 km. It has been shown that ionospheric irregularities produced by auroral electrojet electric field peak around this altitude [Pfaff *et al.*, 1984; Kelly, 1989]

The maps of EICs (Figures 7a and 8a) show that GPS phase scintillation is collocated with the westward electrojet currents with the strongest scintillation mapping to the poleward side of strong westward EICs. In relation to vertical current amplitudes (Figures 7b and 8b) strong scintillation maps to vertical upward or downward  $J_z$  currents, or near the reversal boundaries between downward and upward  $J_z$ . As it would be expected, these are the regions where

strong aurora caused by energetic particle precipitation occurs. For the same time interval, scintillation is found to be collocated with UV aurora observed by DMSP satellites (Figure 9).

Focusing on two 40°-longitude sectors with the best coverage by GPS receivers centered about 280°E and 10° longitudes 15-min averaged EICs and phase scintillation occurrence maps are compared in Figures 10 and 12. It is found that scintillation occurrence in the auroral zone is collocated with the westward electrojet currents, particularly on the poleward side, and with the poleward edge of the eastward electrojet current region. In addition, it is noted that, in general, the energetic electron fluxes observed by DMSP satellites are elevated near the poleward edges of the westward or eastward electrojets, where scintillation occurrence is also elevated. The exception is a one hour interval between 11:00 and 12:00 UT when no scintillation and very weak EICs ( $< 200$  mA/m) were present, yet large fluxes of energetic particles were observed. It is found that during this interval strong pulsating auroras were observed by THEMIS ground-based all-sky imagers and ULF waves were observed by mid-latitude SuperDARN radars.

In summary, GPS scintillation regions at high latitudes, namely, storm enhanced density, cusp, polar cap with either polar patches or sun-aligned arcs, auroral oval and subauroral polarization streams are largely determined by coupling between the solar wind and magnetosphere. In relation to auroral electrojet currents, scintillation maps to strong EICs, particularly to the poleward side of the westward electrojet and to the poleward edge of the eastward electrojet current region. Scintillation was collocated with energetic electron precipitation regions and aurora observed by DMSP satellites with the exception of a period of pulsating aurora and ULF waves, when large fluxes of energetic particles but very weak EICs were observed.

## **Acknowledgments**

Infrastructure funding for CHAIN was provided by the Canada Foundation for Innovation and the New Brunswick Innovation Foundation. CHAIN operation is conducted in collaboration with the Canadian Space Agency (CSA). The magnetometer and riometer operation and data processing were supported by the Geomagnetic Laboratory, Natural Resources Canada. The Virginia Tech authors acknowledge the support of NSF Awards AGS-0838219 and AGS-0946900. The authors acknowledge the use of SuperDARN data. SuperDARN is a collection of radars funded by national scientific funding agencies of Australia, Canada, China, France, Japan, South Africa, the United Kingdom, and the United States of America. IMAGE magnetometer data are provided by several institutes from Finland, Norway, Sweden, Poland and Russia. The DMSP particle detectors were designed by Dave Hardy of AFRL, and data obtained from JHU/APL. International GNSS Service (IGS) and its contributing organizations, including the Denmark Technical University National Space Institute, are gratefully acknowledged for contributing 1-Hz GPS data. The Norwegian Mapping Authority provided data obtained by a national real-time kinematic positioning network. Data contributed by the Nottingham Geospatial Institute is from a network of GNSS receivers established through a research grant by the UK Engineering and Physical Sciences Research Council (EPSRC grant number: EP/H003479/1). KO is supported by the Research Council of Norway under contracts 212014 and 223252. We thank the many different groups operating magnetometer arrays for providing data for this study including: the THEMIS UCLA magnetometer network (Ground-based Imager and Magnetometer Network for Auroral Studies) is funded through NSF grant AGS-1004736. AUTUMNX magnetometer network is funded through the Canadian Space Agency/Geospace Observatory (GO) Canada program Athabasca University, Centre for Science/Faculty of Science and Technology. The Canadian Space Science Data Portal is funded in part by the Canadian Space Agency contract numbers 9F007-071429 and 9F007-070993. The Canadian Magnetic Observatory Network (CANMON) is maintained and operated by the Geological Survey of Canada - <http://gsc.nrcan.gc.ca/geomag>. The Magnetometer Array for Cusp and Cleft Studies (MACCS) array is supported by US National Science Foundation grant ATM-0827903 to Augsburg College. The McMAC Project is sponsored by the Magnetospheric Physics Program of National Science Foundation through grant AGS-0245139 and maintained by Dr. Peter Chi. We would like to thank the following: Jürgen Matzka for calibrating the DTU

magnetometers; M. J. Engebretson, D. Murr, and E.S. Steinmetz at Augsburg College; and the MACCS team. The Solar and Terrestrial Physics (STEP) magnetometer file storage is at the Department of Earth and Planetary Physics, University of Tokyo and maintained by Dr. Kanji Hayashi (hayashi@grl.s.u-tokyo.ac.jp). The USGS Geomagnetism Program. This work was supported by the Public Safety Geosciences program of the Natural Resources Canada, Earth Sciences Sector (NRCan ESS Contribution 20160133).

## References

- Aarons, J. (1997), Global positioning system phase fluctuations at auroral latitudes, *J. Geophys. Res.*, *102*(A8), 17219–17231.
- Aarons J., B. Lin, M. Mendillo, K. Liou, and M. Codrescu (2000), Global Positioning System phase fluctuations and ultraviolet images from the Polar satellite, *J. Geophys. Res.*, *105*(A3), 5201–5213.
- Amm, O., and A. Viljanen (1999), Ionospheric disturbance magnetic field continuation from the ground to the ionosphere using spherical elementary currents systems, *Earth Planets Space*, *51*, 431–440.
- Aquino, M., A. Dodson, J. Souter, and T. Moore (2007) Ionospheric scintillation effects on GPS carrier phase positioning accuracy at auroral and sub-auroral latitudes, in *Dynamic Planet, International Association of Geodesy Symposia*, vol. 130, edited by M. Aquino et al., pp. 859–866, Springer, Berlin, doi:10.1007/978-3-540-49350-1\_121.
- Basu, S., E. M. MacKenzie, Su. Basu, E. Costa, P. F. Fougere, H. C. Carlson, Jr., and H. E. Whitney (1987), 250 MHz/GHz scintillation parameters in the equatorial, polar, and auroral environments, *IEEE J. Select. Areas Commun.*, *2*(2), 102–115.
- Basu, S., Su. Basu, J. J. Sojka, R. W. Schunk, and E. MacKenzie (1995), Macroscale modeling and mesoscale observations of plasma density structures in the polar cap, *Geophys. Res. Lett.*, *22*(8), 881–884.
- Basu, S., E. J. Weber, T. W. Bullett, M. J. Keskinen, E. MacKenzie, P. Doherty, R. Sheehan, H. Kuenzler, P. Ning, and J. Bongiolatti (1998), Characteristics of plasma structuring in the cusp/cleft region at Svalbard, *Radio. Sci.*, *33*(6), 1885–1899.
- Cherniak, I., I. Zakharenkova, and R. J. Redmon (2015), Dynamics of the high-latitude ionospheric irregularities during the 17 March 2015 St. Patrick’s Day storm: Ground-based GPS measurements, *Space Weather*, *13*, 585–597, doi:10.1002/2015SW001237.
- Chisham, G., M. Lester, S. E. Milan, M. P. Freeman, W. A. Bristow, A. Grocott, K. A. McWilliams, J. M. Ruohoniemi, T. K. Yeoman, P. L. Dyson, R. A. Greenwald, T. Kikuchi, M. Pinnock, J. P. S. Rash, N. Sato, G. J. Sofko, J. P. Villain, and A. D. M. Walker (2007), A

decade of the Super Dual Auroral Radar Network (SuperDARN): Scientific achievements, new techniques and future directions, *Survey Geophys.*, 28, 33–109.

de Paula, E. R., O. F. Jonah, A. O. Moraes, E. A. Kherani, B. G. Fejer, M. A. Abdu, M. T. A. H. Muella, I. S. Batista, S. L. G. Dutra, and R. R. Paes (2015), Low-latitude scintillation weakening during sudden stratospheric warming events, *J. Geophys. Res. Space Physics*, 120, doi:10.1002/2014JA020731.

Ghoddousi-Fard R. and F. Lahaye (2016), Evaluation of single frequency GPS precise point positioning assisted with external ionosphere sources. vol. 57, pp. 2154-2166, *Adv. Space Res.* doi: 10.1016/j.asr.2016.02.017.

Ghoddousi-Fard R., P. Prikryl, and F. Lahaye (2013). GPS phase difference variation statistics: A comparison between phase scintillation index and proxy indices. *Adv. Space Res.*, 52, 1397-1405, doi: 10.1016/j.asr.2013.06.035.

Ghoddousi-Fard R., P. Héroux, D. Danskin, and D. Boteler (2011), Developing a GPS TEC Mapping Service over Canada, *Space Weather*, Vol. 9, S06D11, doi: 10.1029/2010SW000621.

Ghoddousi-Fard, R., L. Nikitina, D. Danskin, P. Prikryl (2015), Analysis of GPS phase rate variations in response to geomagnetic field perturbations over the Canadian auroral region, *Adv. Space Res.*, Vol.55, issue 5, p.1372-1381, doi: 10.1016/j.asr.2014.12.021.

Greenwald, R. A., K. B. Baker, J. R. Dudeney, M. Pinnock, T. B. Jones, E. C. Thomas, J.-P. Villain, J.- C. Cerrisier, C. Senior, C. Hanuise, R. D. Hunsucker, G. Sofko, J. Koehler, E. Nielsen, R. Pellinen, A. D. M. Walker, N. Sato, and H. Yamagishi (1995), DARN/SUPERDARN: A global view of the dynamics of high- latitude convection, *Space Sci. Rev.*, 71, 761–796.

Holzworth, R.H. and C.-I. Meng (1975) Mathematical Representation of the Auroral Oval, *Geophysical Research Letters*, 2(9), 377-380.

Imber, S. M., S. E. Milan, and M. Lester (2013), The Heppner-Maynard Boundary measured by SuperDARN as a proxy for the latitude of the auroral oval, *J. Geophys. Res. Space Physics*, 118, 685–697, doi:10.1029/2012JA018222.

Jacobsen, K. S., and M. Dähnn (2014), Statistics of ionospheric disturbances and their correlation with GNSS 338 positioning errors at high latitudes. *J. Space Weather Space Clim.*, 4, A27, 2014. 10.1051/swsc/2014024, <http://dx.doi.org/10.1051/swsc/2014024>.

Jacobsen, K. S., and Y. L. Andalsvik (2016), Overview of the 2015 St. Patrick's day storm and its consequences for RTK and PPP positioning in Norway, *J. Space Weather Space Clim.*, 6, A9, <http://dx.doi.org/10.1051/swsc/2016004>.

Jayachandran P. T., et al. (2009), Canadian High Arctic Ionospheric Network (CHAIN). *Radio Sci* 44:RS0A03. doi:10.1029/2008RS004046 [printed 45(1), 2010].

Jin, Y., J. I. Moen, and W. J. Miloch (2015), On the collocation of the cusp aurora and the GPS phase scintillation: A statistical study, *J. Geophys. Res. Space Physics*, 120, 9176–9191, doi:10.1002/2015JA021449.

Kamide, Y., and K. Kusano (2015), No Major Solar Flares but the Largest Geomagnetic Storm in the Present Solar Cycle, *Space Weather*, 13, 365–367, doi:10.1002/2015SW001213.

Kataoka, R., D. Shiota, E. Kilpua, and K. Keika (2015), Pileup accident hypothesis of magnetic storm on 17 March 2015, *Geophys. Res. Lett.*, 42, 5155–5161, doi:10.1002/2015GL064816.

Kelly, M.C. (1989), *The Earth's Ionosphere: Plasma Physics and Electrodynamics*. Academic Press Inc., San Diego.

Kinrade, J., C. N. Mitchell, N. D. Smith, Y. Ebihara, A. T. Weatherwax, and G. S. Bust (2013), GPS phase scintillation associated with optical auroral emissions: First statistical results from the geographic South Pole, *J. Geophys. Res. Space Phys.*, 118, 2490–2502.

Kintner, P. M., B. M. Ledvina, and E. R. de Paula (2007), GPS and ionospheric scintillations, *Space Weather*, 5, S09003, doi:10.1029/2006SW000260.

Laundal, K. M., et al. (2015), Birkeland current effects on high-latitude ground magnetic field perturbations, *Geophys. Res. Lett.*, 42, 7248–7254, doi:10.1002/2015GL065776.

Li, G., B. Baiqi Ning, Z. Ren, L. Lianhuan Hu (2010), Statistics of GPS ionospheric scintillation and irregularities over polar regions at solar minimum, *GPS Solut.*, DOI 10.1007/s10291-009-0156-x.

Liu, W.W. (2005), Canadian space environment program and international living with a star, *Adv. Space Res.*, 35(1), 51–60.

Mann, I., R., D. K. Milling, I. J. Rae, L. G. Ozeke, A. Kale, Z. C. Kale, K. R. Murphy, A. Parent, M. Usanova, D. M. Pahud, V. Lee, E.-A. Amalraj, D. D. Wallis, V. Angelopoulos, K.-H. Glassmeier, C. T. Russell, H.-U. Auster, and H. J. Singer (2008), The Upgraded CARISMA Magnetometer Array in the THEMIS Era, *Space Sci. Rev.*, 141(1–4), 413–451, doi:10.1007/s11214-008-9457-6.

Mende, S., S. Harris, H. Frey, V. Angelopoulos, C. Russell, E. Donovan, B. Jackel, M. Greffen, and L. Peticolas (2008), The THEMIS array of ground-based observatories for the study of auroral substorms, *Space Sci. Rev.*, 141, 357–387, doi:10.1007/s11214-008-9380-x.

Moen, J., K. Oksavik, L. Alfonsi, Y. Daabakk, V. Romano, and L. Spogli (2013), Space weather challenges of the polar cap ionosphere, *J. Space Weather Space Clim.*, 3, A02, DOI: 10.1051/swsc/2013025.

Oksavik, K., C. van der Meeren, D. A. Lorentzen, L. J. Baddeley, and J. Moen (2015), Scintillation and loss of signal lock from poleward moving auroral forms in the cusp ionosphere, *J. Geophys. Res. Space Physics*, 120, 9161–9175, doi:10.1002/2015JA021528.

Paxton, L.J., D. Morrison, Y. Zhang, H. Kil, B. Wolven, B.S. Ogorzalek, D.C. Humm, and C.-I. Meng (2002), Validation of remote sensing products produced by the Special Sensor Ultraviolet Scanning Imager (SSUSI) – a far-UV imaging spectrograph on DMSP F16, *Proc. SPIE*, 4485, 338.

Pfaff, R. F., M. C. Kelley, B. G. Fejer, E. Kudeki, C. W. Carlson, A. Pedersen, and B. Hausler (1984), Electric field and plasma density measurements in the auroral electrojet, *J. Geophys. Res.*, 89(A1), 236–244.

Prikryl, P., P. T. Jayachandran, S. C. Mushini, and R. Chadwick (2011a), Climatology of GPS phase scintillation and HF radar backscatter for the high-latitude ionosphere under solar minimum conditions, *Ann. Geophys.*, 29, 377–392.

Prikryl, P., L. Spogli, P. T. Jayachandran, J. Kinrade, C. N. Mitchell, B. Ning, G. Li, P. J. Cilliers, M. Terkildsen, D. W. Danskin, E. Spanswick, E. Donovan, A. T. Weatherwax, W. A. Bristow, L. Alfonsi, G. De Franceschi, V. Romano, C. M. Ngwira, and B. D. L. Opperman (2011b), Interhemispheric comparison of GPS phase scintillation at high latitudes during the magnetic cloud-induced geomagnetic storm of 5–7 April 2010, *Ann. Geophys.*, 29, 2287–2304.

Prikryl, P., R. Ghoddousi-Fard, B. S. R. Kunduri, E. G. Thomas, A. J. Coster, P. T. Jayachandran, E. Spanswick, and D. W. Danskin (2013a), GPS phase scintillation and proxy index at high latitudes during a moderate geomagnetic storm, *Ann. Geophys.*, 31, 805–816.

Prikryl, P., Y. Zhang, Y. Ebihara, R. Ghoddousi-Fard, P. T. Jayachandran, J. Kinrade, C. N. Mitchell, A. T. Weatherwax, G. Bust, P. J. Cilliers, L. Spogli, L. Alfonsi, G. De Franceschi, V. Romano, B. Ning, G. Li, M. J. Jarvis, D. W. Danskin, E. Spanswick, E. Donovan, and M. Terkildsen (2013b), An interhemispheric comparison of GPS phase scintillation with auroral emission observed at South Pole and from DMSP satellite, *Ann. Geophys. (Special Issue)*, 56, 2, R0216; doi:10.4401/ag-6227.

Prikryl, P., P. T. Jayachandran, S. C. Mushini, and I. G. Richardson (2014), High-Latitude GPS phase scintillation and cycle slips during high speed solar wind streams and interplanetary coronal mass ejections: A superposed epoch analysis, *Earth Planets Space*, 66, 62 doi:10.1186/1880-5981-66-62.

Prikryl, P., P. T. Jayachandran, R. Chadwick, and T. D. Kelly (2015a), Climatology of GPS phase scintillation at northern high latitudes for the period from 2008 to 2013, *Ann. Geophys.*, 33, 531-545, doi:10.5194/angeo-33-531-2015.

Prikryl, P., R. Ghoddousi-Fard, E. G. Thomas, J. M. Ruohoniemi, S. G. Shepherd, P. T. Jayachandran, D. W. Danskin, E. Spanswick, Y. Zhang, Y. Jiao, and Y. T. Morton (2015b), GPS phase scintillation at high latitudes during geomagnetic storms of 7–17 March 2012 – Part 1: The North American sector, *Ann. Geophys.*, 33, 637-656, doi:10.5194/angeo-33-637-2015.

Prikryl, P., R. Ghoddousi-Fard, J. M. Ruohoniemi, E. G. Thomas (2015c), GPS phase scintillation at high latitudes during two geomagnetic storms, Accepted for publication in *Auroral dynamics and space weather*, Zhang, Y. and Paxton, L.J. (Editors), AGU, Wiley Publ.

Skone, S., M.E. Cannon (1999), Ionospheric effects on differential GPS applications during auroral substorm activity. *J. ISPRS* 54 (4), 279–288.

Skone, S., and M. de Jong (2000), The impact of geomagnetic substorms on GPS receiver performance, *Earth Planets Space*, 52, 1067–1071.

Skone, S., F. Man, F. Ghafoori, and R. Tiwari (2008), Investigation of Scintillation Characteristics for High Latitude Phenomena, ION GNSS 2008, Session D5, Savannah, GA, 16-19 September 2008.

Spogli, L., L. Alfonsi, G. De Franceschi, V. Romano, M. H. O. Aquino, and A. Dodson, (2009), Climatology of GPS ionospheric scintillations over high and mid-latitude European regions, *Ann. Geophys.*, 27, 3429–3437.

Sreeja, V., T. K. Pant, L. Jose, and S. Ravindran (2011), Westward electric field penetration to the dayside equatorial ionosphere during the main phase of the geomagnetic storm on 22 July 2009, *J. Geophys. Res.*, 116, A03303, doi:10.1029/2010JA016013.

Sreeja, V. and M. Aquino (2014), Statistics of ionospheric scintillation occurrence over European High latitudes, *J. Atmos. Solar-Terrest. Phys.*, 120, doi:10.1016/j.jastp.2014.09.003

Thomas, E. G., J. B. H. Baker, J. M. Ruohoniemi, L. B. N. Clausen, A. J. Coster, J. C. Foster, and P. J. Erickson (2013), Direct observations of the role of convection electric field in the formation of a polar tongue of ionization from storm enhanced density, *J. Geophys. Res. Space Phys.*, 118, 1180–1189.

van der Meeren, C., K. Oksavik, D. Lorentzen, J. I. Moen, and V. Romano (2014), GPS scintillation and irregularities at the front of an ionization tongue in the nightside polar ionosphere, *J. Geophys. Res. Space Physics*, 119, 8624–8636, doi:10.1002/2014JA020114.

van der Meeren, C., K. Oksavik, D. A. Lorentzen, M. T. Rietveld, and L. B. N. Clausen (2015), Severe and localized GNSS scintillation at the poleward edge of the nightside auroral oval during intense substorm aurora, *J. Geophys. Res. Space Physics*, 120, 10,607–10,621, doi:10.1002/2015JA021819.

Weygand, J. M., O. Amm, A. Viljanen, V. Angelopoulos, D. Murr, M. J. Engebretson, H. Gleisner, and I. Mann (2011), Application and validation of the spherical elementary currents systems technique for deriving ionospheric equivalent currents with the North American and Greenland ground magnetometer arrays, *J. Geophys. Res.*, 116, A03305, doi:10.1029/2010JA016177.

Weygand, J. M. and S. Wing (2016), Comparison of DMSP and SECS region-1 and region-2 ionospheric current boundary, *J. Atmos. Solar-Terr. Phys.*, 143-144, 8–13, <http://dx.doi.org/10.1016/j.jastp.2016.03.002>.

Zhang, Y. and L.J. Paxton (2008), An empirical K<sub>p</sub>-dependent global auroral model based on TIMED/GUVI FUV data, *J. Atmos. Solar-Terrest. Phys.*, 70, 1231-1242.

### GISTMs complemented by 1Hz GPS receivers

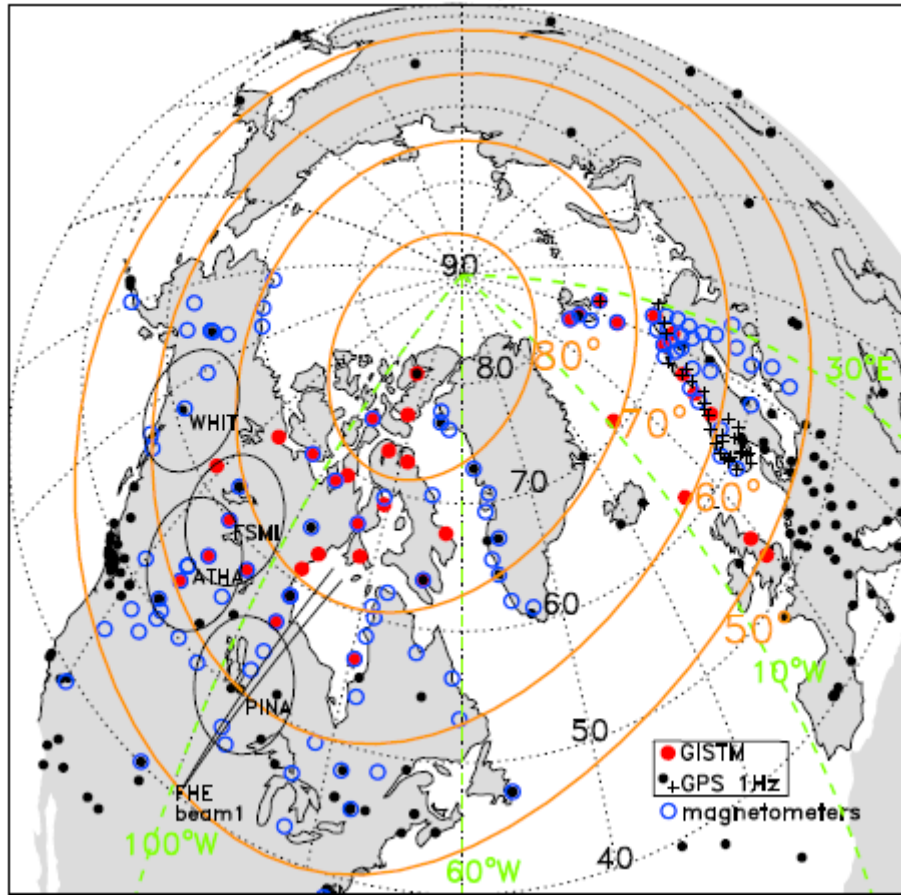


**Figure 1.** The Canadian High Arctic Ionospheric Network (CHAIN) complemented by GISTMs in the North European sector and GPS receivers recording at a sampling rate of 1 Hz. Red dots show locations of specialized scintillation receivers (GISTMs). Black dots show locations of 1-Hz GPS receivers, mainly from IGS and GNET. Black crosses show a fraction of 1-Hz receivers that are a part of the NMA network. Ground magnetometers used to obtain EICs are shown as blue open circles. The AACGM latitudes 50°, 60°, 70° and 80°, in yellow, are superposed over the geographic grid. The dashed green lines delineate two 40°-wide longitude sectors discussed in the text. Field-of-views of four THEMIS ASIs and beam 1 of the SuperDARN Fort Hays East radar are shown.

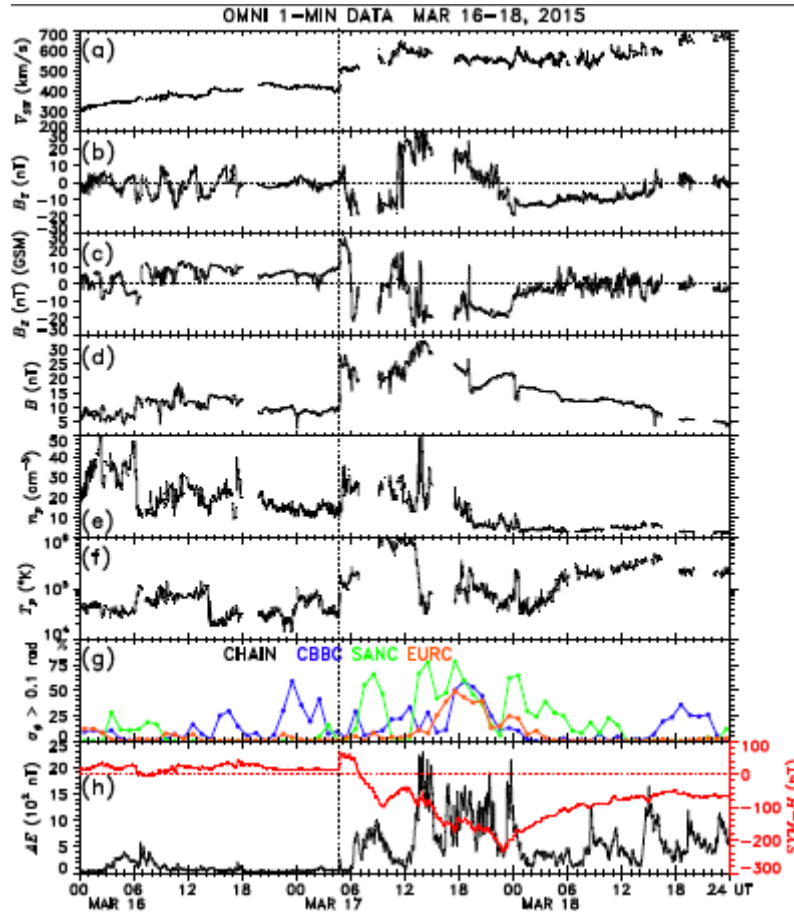


**Figure 2.** (a-f) The solar wind data from the 5-min OMNI data set from March 16 to 18, 2015. (g) The hourly occurrence of phase scintillation ( $\sigma_\phi > 0.1$  rad) observed by CHAIN in Cambridge Bay (CBBC), Eureka (EURC) and Sanikiluaq (SANC), and (h) provisional geomagnetic indices  $AE$  and  $SYM-H$  are also shown. An interplanetary shock is shown by vertical dotted line.

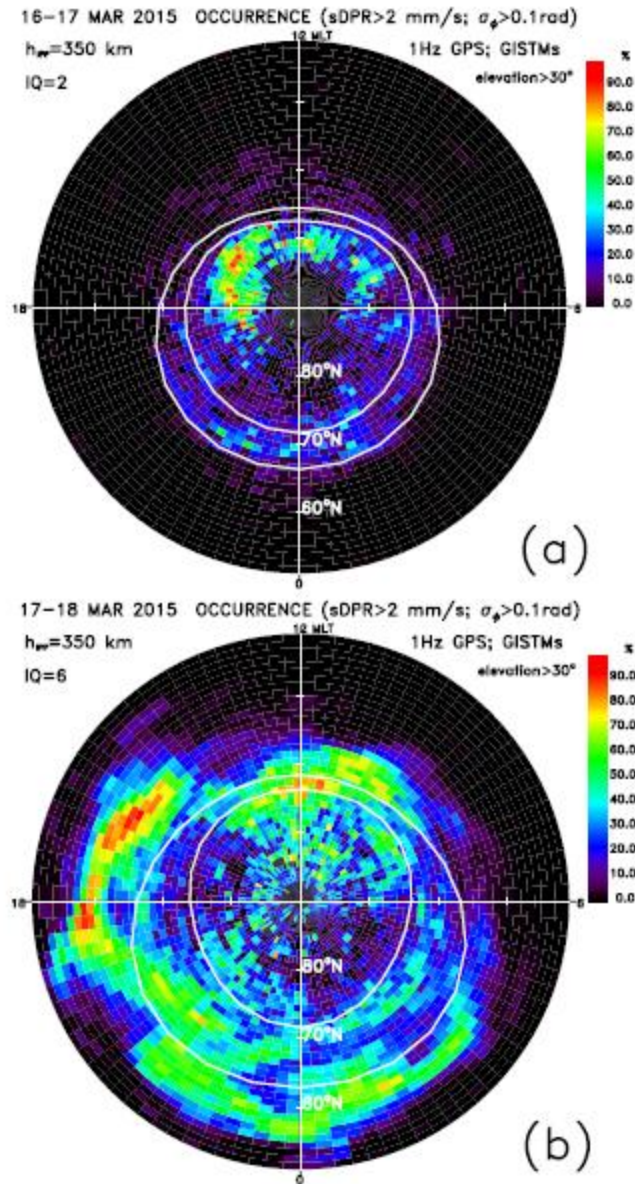


**Figure 3.** The phase scintillation occurrence of  $\sigma_\phi > 0.1$  rad or  $sDPR > 2$  mm/s for CHAIN combined with 1-Hz GPS receivers for data from (a) 04:00 UT on March 16 to 03:59 UT on March 17 and (b) 04:00 UT on March 17 to 03:59 UT on March 18, 2015. The scintillation occurrence is mapped in coordinates of AACGM latitude and MLT. Boundaries of the statistical auroral oval are shown.

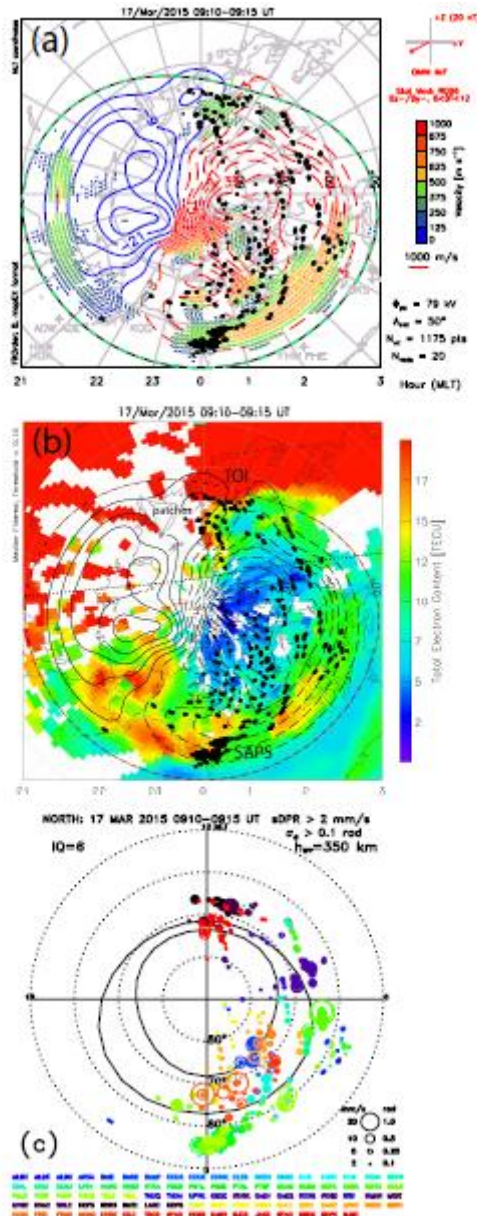


**Figure 4.** (a) SuperDARN convection and potential maps showing expanded convection zone and (b) the 5-min median-filtered TEC mapped in coordinates of AACGM latitude and MLT at 09:10 UT on March 17. In (a) and (b) IPPs with  $\sigma_\phi > 0.1$  rad or  $sDPR > 2$  mm/s are superposed (black dots). (c) The same IPPs are shown as circles that are sized proportionally to  $\sigma_\phi$  and  $sDPR$  values. Individual stations and their code names are distinguished by color. The IPPs for the IGS 1-Hz GPS receivers are shown in blue, cyan and green, followed by GNET in dark blue and purple, and the NMA 1-Hz receiver array in black. CHAIN is shown in yellow and orange, and the European GISTMs in red.

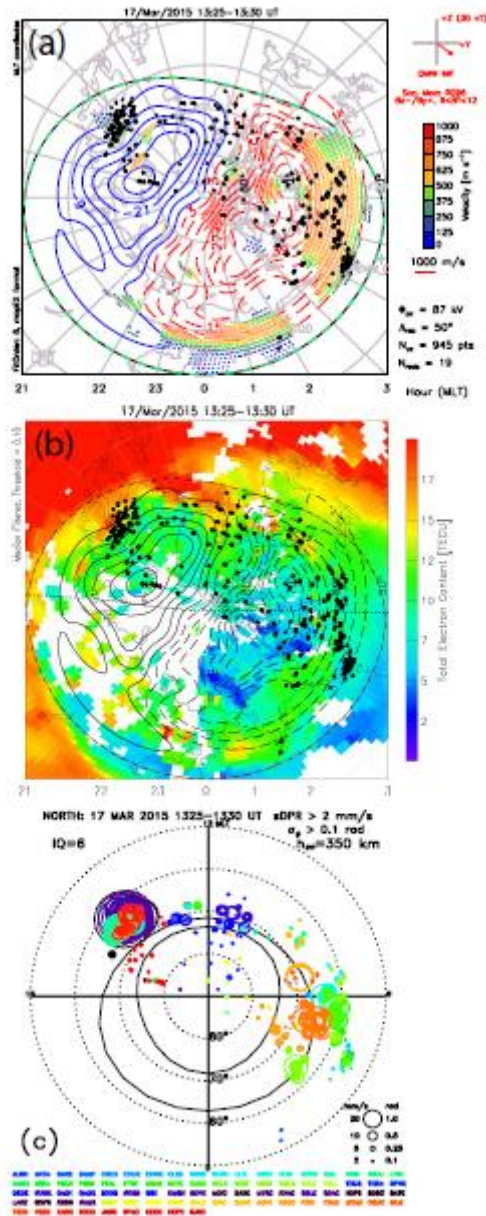


**Figure 5.** (a) SuperDARN convection and potential maps showing an expanded convection zone and (b) the 5-min median-filtered TEC mapped in coordinates of AACGM latitude and MLT at 13:25 UT on March 17. In (a) and (b) IPPs with  $\sigma_\phi > 0.1$  rad or  $sDPR > 2$  mm/s are superposed (black dots). (c) The same IPPs are shown as circles that are sized proportionally to  $\sigma_\phi$  and  $sDPR$  values.

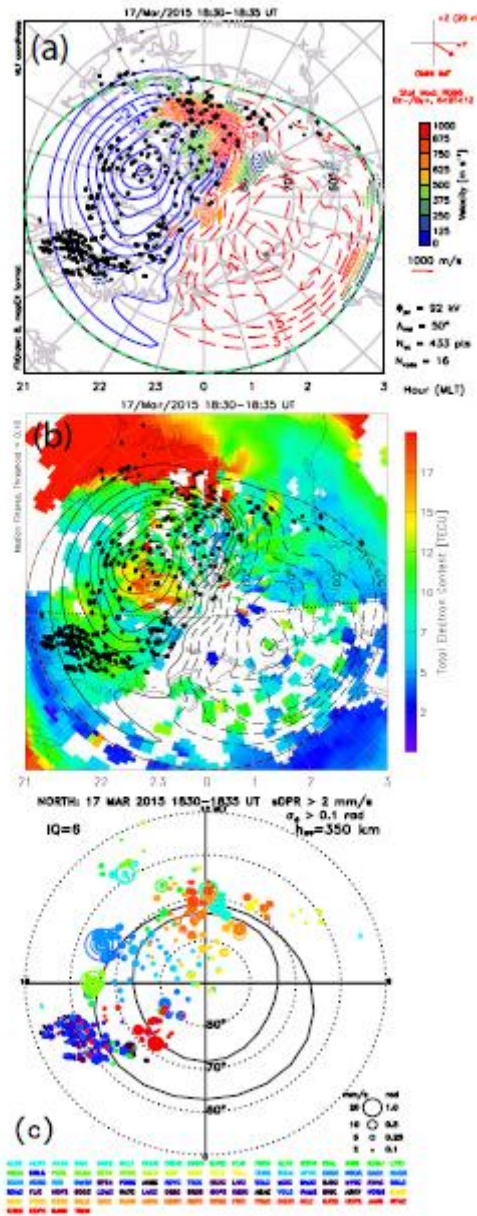


**Figure 6.** The same as Figure 4 but at 18:00 UT on March 17.

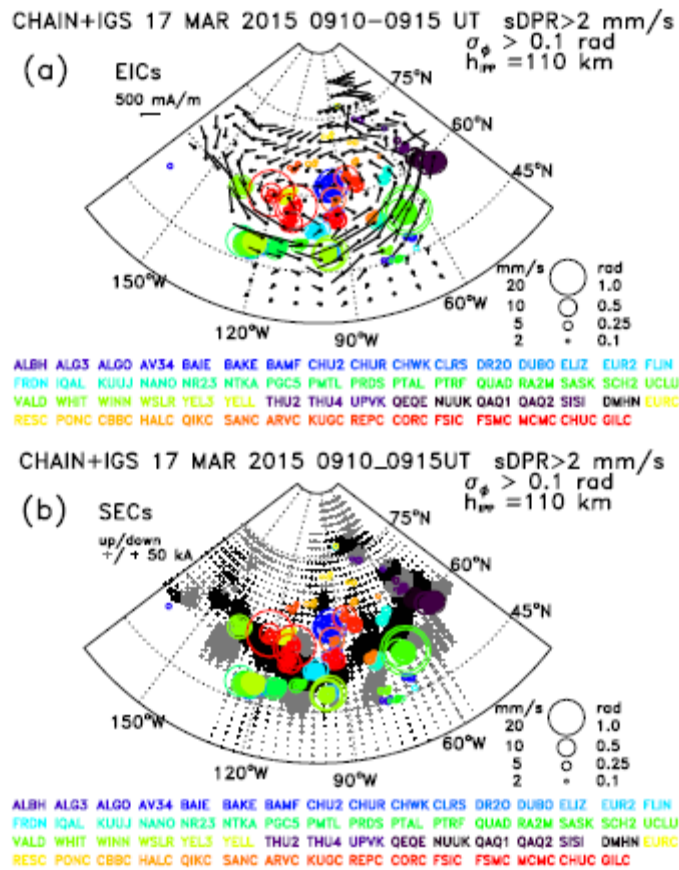


**Figure 7.** (a) Horizontal equivalent ionospheric currents (EICs) and (b) vertical current amplitudes (SECS) observed over North America on 17 March 2015 at 09:10 UT. Ionospheric pierce points where  $\sigma_{\phi} > 0.1$  rad or sDPR  $> 2$  mm/s are superposed as circles color-coded by stations and sized proportionally to  $\sigma_{\phi}$  and sDPR values.

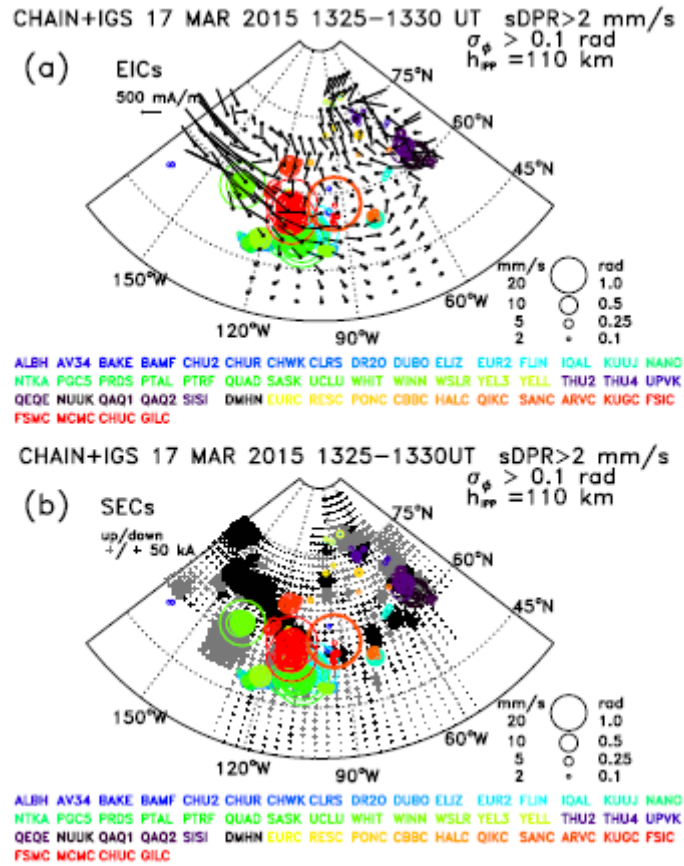


**Figure 8.** The same as Figure 7 except at 13:25 – 13:30 UT.

March 17, 2015 DOY:076 Orbit: 43155 (DMSP F17)

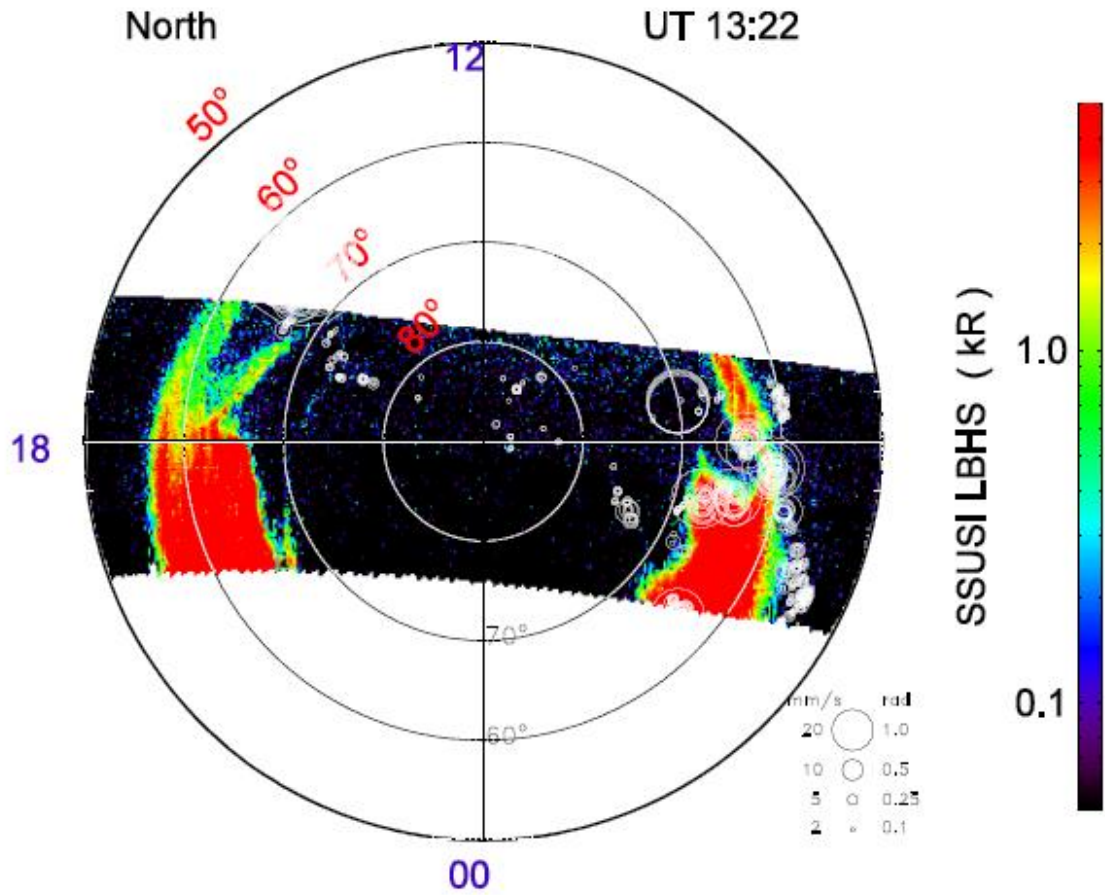


**Figure 9.** SSUSI (DMSP F17) auroral image scans mapped as a function of AACGM latitude and MLT. Scintillation IPPs are shown as white open circles that are scaled by the scintillation intensity.

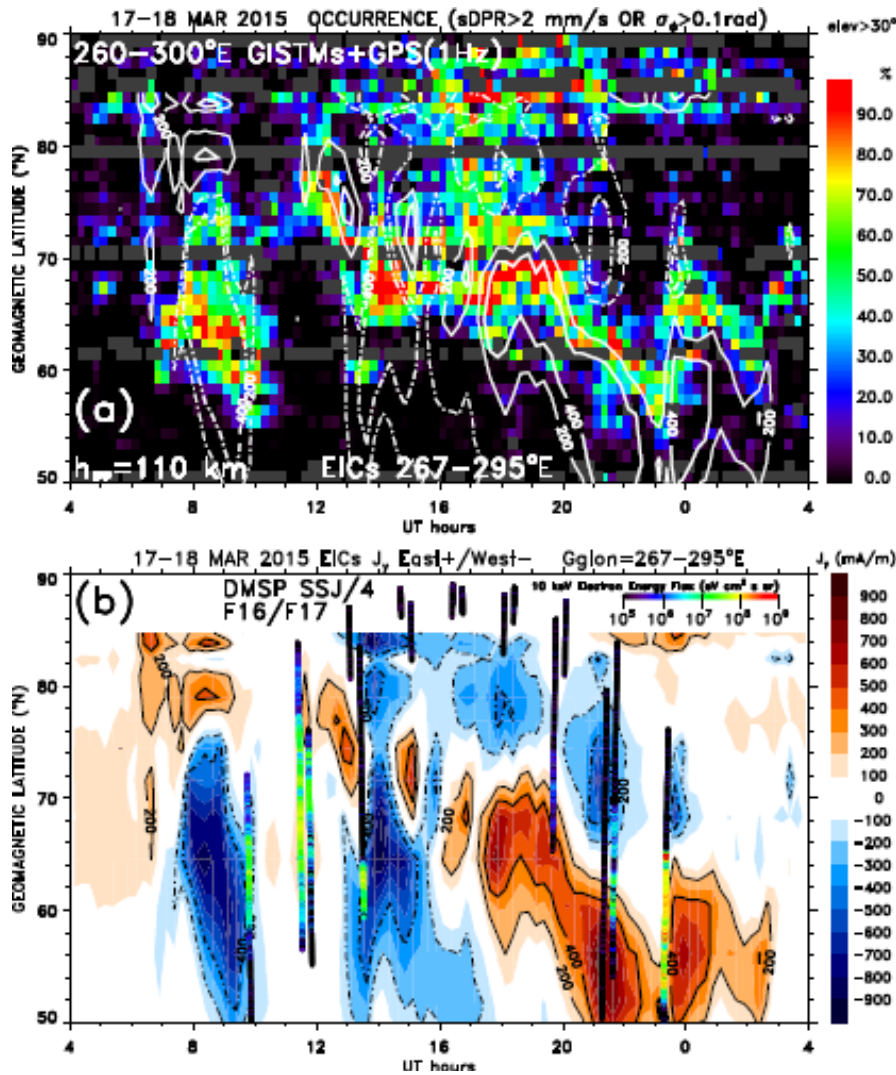


**Figure 10.** (a) The phase scintillation occurrence of  $\sigma_\phi > 0.1$  rad or sDPR  $> 2$  mm/s as a function of AAGCM latitude and UT for CHAIN combined with 1-Hz GPS receivers for data from 04:00 UT on March 17 to 03:59 UT on March 18, 2015. Contour plots of the westward and eastward equivalent ionospheric currents are shown in white broken and solid lines, respectively. (b) Westward and eastward equivalent ionospheric currents are highlighted in blue and brown shades. Superposed are tracks of DMSP F16 and F17 satellites that crossed the longitude sector between 260° and 300°. The tracks are color-coded with observed energy flux of 10 keV electrons.

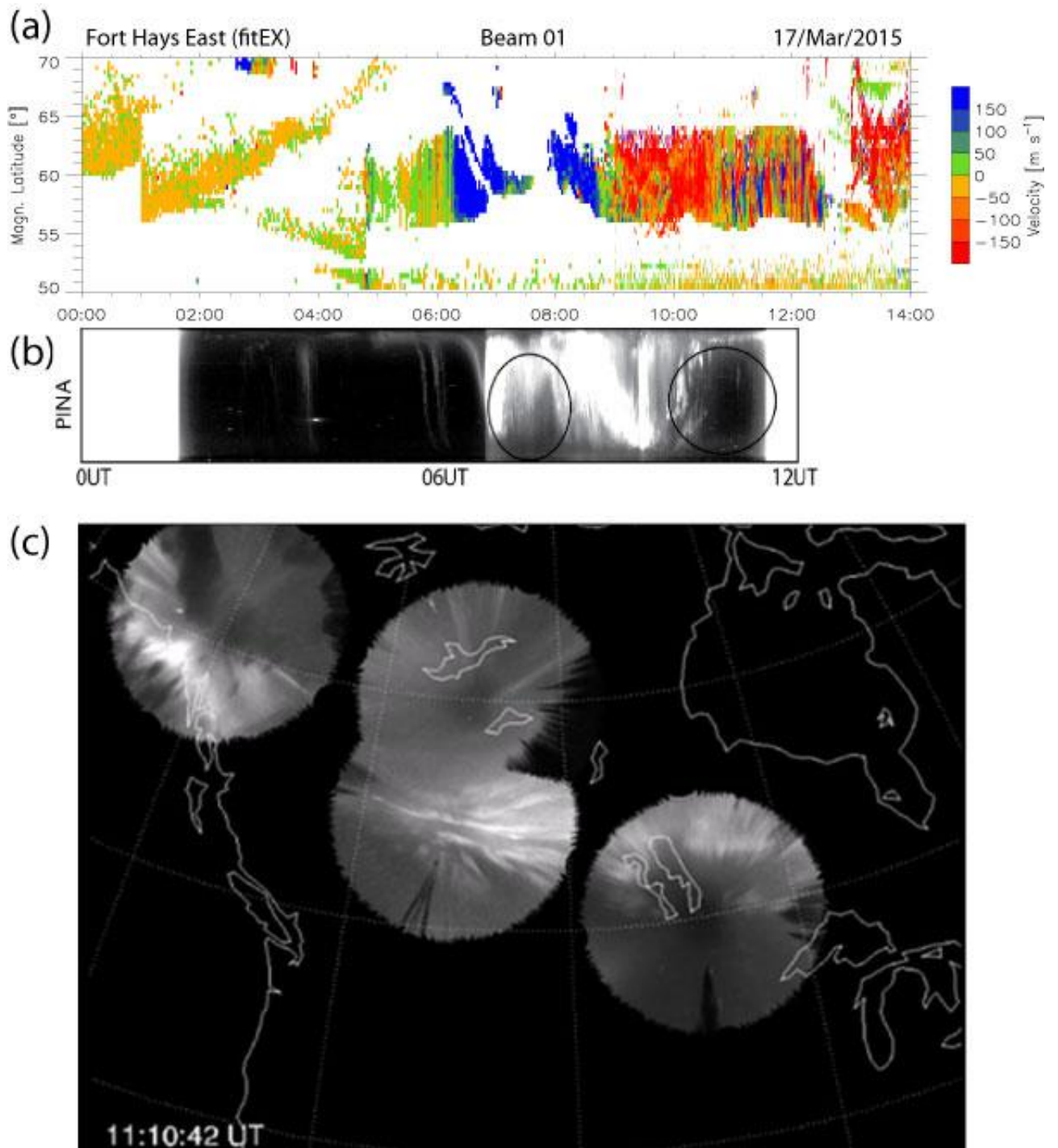


**Figure 11.** (a) Fort Hays East radar line-of-sight velocity for beam 1. (b) Keogram of aurora observed by THEMIS ASI in Pinawa with circles approximately indicating occurrence of pulsating aurora. (c) THEMIS all-sky imagers showing pulsating aurora at 11:10 UT.

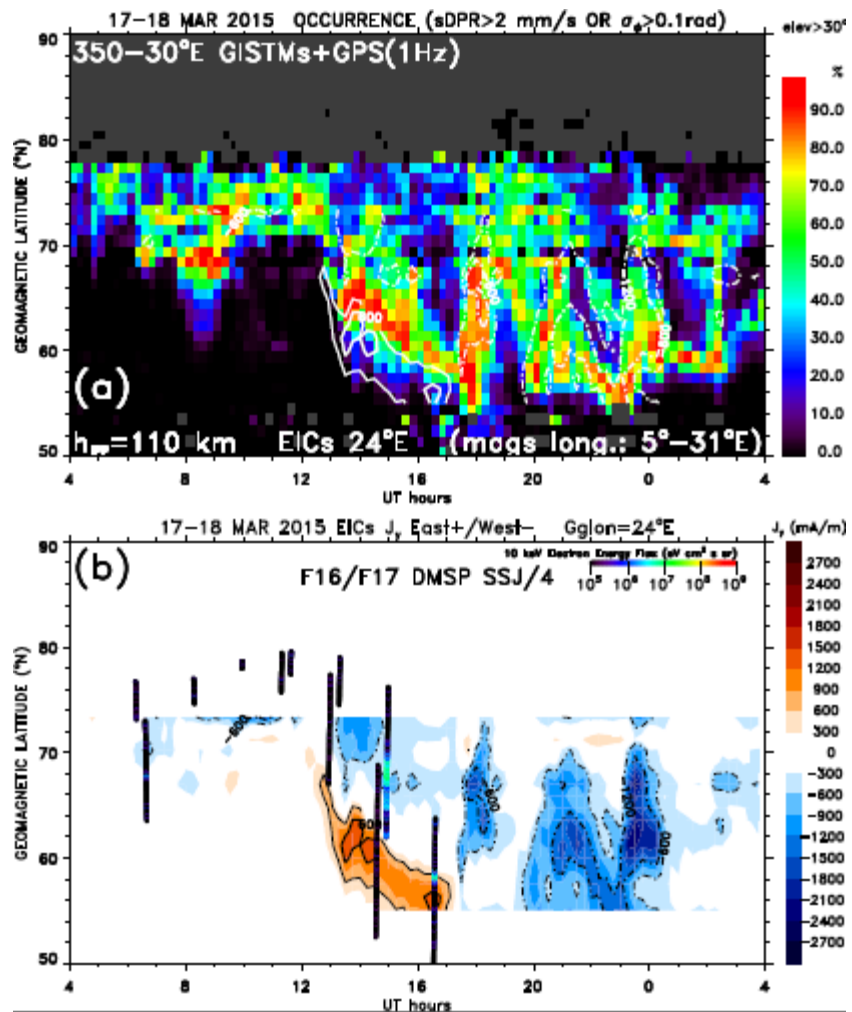


**Figure 12.** The same as Figure 10 except for (a) the scintillation longitude sector between 350° and 30° and (b) the EICs for the longitude 24°.